Journal of Materials Research and Technology 37 (2025) 1970–1986

Contents lists available at ScienceDirect

Journal of Materials Research and Technology

journal homepage: www.elsevier.com/locate/jmrt

Influence of laser beam shape and post heat-treatment on the microstructure and mechanical properties of nickel-based alloy IN718 manufactured by laser powder bed fusion

Matjaž Godec [a,*,1], Narges Mirzabeigi [b,c,1], Črtomir Donik [a], Danijela A. Skobir Balantič [a], Simon Malej [a], Irena Paulin [a], Bojan Podgornik [a], Jonas Grünewald [b], Tobias Novotny [c], Florian Bayer [c], Francisco Ruiz-Zepeda [a,d], Katrin Wudy [b]

[a] Institute of Metals and Technology, Ljubljana, Slovenia
[b] Technical University of Munich, Munich, Germany
[c] EOS GmbH Electro Optical Systems, Munich, Germany
[d] National Institute of Chemistry, Ljubljana, Slovenia

ARTICLE INFO

Keywords:
PBF-LB/M
Beam shaping
IN718
Heat treatment
Mechanical properties

ABSTRACT

This study examines the effect of Gaussian and ring-shaped laser beam profiles on the microstructural development and mechanical properties of the PBF-LB/M processed nickel-based alloy Inconel 718 in its as-built and post-heat-treated conditions. Beam shaping was employed to achieve a faster build rate without compromising material properties. One of the objectives was to optimise heat treatment conditions for the beam-shaped profile. The post-heat-treatment process included four different solution annealing temperatures (954 °C, 984 °C, 1034 °C and 1154 °C), followed by two-step ageing, respectively. The microstructure evolution was revealed using scanning electron microscopy (SEM) equipped with energy-dispersive X-ray diffraction (EDS). The mechanical properties in all investigated conditions were evaluated based on tensile tests at room temperature. Using a Gaussian laser beam profile results in a fine-grained microstructure without a strong columnar orientation, while the ring beam profile produces a distinct columnar structure with larger nanodendritic grains and dislocation cells. Both beam profiles exhibit a similar proportion of Laves phase. After post-heat treatment, the Gaussian beam profile generally provides 3–7 % higher mechanical properties. The differences in mechanical properties between horizontal and vertical building directions are greater for ring-shaped laser beam profiles. Heat-treatment temperature above 1034 °C leads to recrystallisation, grain growth and the formation of carbonitrides which reduce mechanical properties. Based on the results, the proposed optimal heat-treatment temperature for both investigated laser beam shapes is 984 °C. At this temperature, tensile strength equalises between horizontal and vertical build directions while yield strength increases, which is beneficial for most applications.

1. Introduction

Nickel-based superalloys are, due to their exceptional mechanical properties at elevated temperatures, extensively used for demanding applications in many industries, such as aerospace, nuclear, and other energy generation fields [1–3]. Among them, Inconel 718 (IN718) and its variants have proven to be the most promising and widely used Ni-based superalloys with great potential further enhanced by their viability for additive manufacturing (AM). AM technologies have become the preferred production routes of complex metallic structures in the last decade due to their ability to manufacture near-net shape components at minimum material waste. They are, therefore, particularly suitable for rapid prototyping and production of critical components. In laser-based powder bed fusion of metals (PBF-LB/M as defined by ISO/ASTM 52900 [4]) a focused laser beam with a Gaussian intensity profile is used as a beam source for melting the powder layer-by-layer.

* Corresponding author.
E-mail address: matjaz.godec@imt.si (M. Godec).
[1] Shared co-first authorship.

https://doi.org/10.1016/j.jmrt.2025.06.119
Received 8 January 2025; Received in revised form 15 June 2025; Accepted 16 June 2025
Available online 18 June 2025

The PBF-LB/M process, characterised by high-temperature gradients, rapid solidification, remelting and reheating of previously deposited layers, strongly affects the morphology and the microstructure of as-build parts, which differ considerably from those of conventionally made products [5]. On the other hand, the mechanical properties of parts produced by conventional methods and PBF-LB/M are generally comparable, although these properties can be significantly influenced by post-processing heat treatment [6].

The microstructure of PBF-LB/M IN718 alloys consists of γ-phase matrix strengthened by two types of precipitates, γ′−Ni_3(Al, Ti) and γ′′−Ni_3Nb which are responsible for the room and high-temperature strength [2]. The properties of PBF-LB/M IN718 strongly depend on PBF-LB/M process parameters, which influence the solidification characteristics and, thus, microstructure [7]. During rapid solidification, Nb, Mo, Ti and C elements segregate at the interdendritic areas. These microsegregations stabilise the formation of specific phases, such as the Laves phase and the MC-type carbides [2,8]. Laves phase (Ni,Fe, Cr)$_2$(Nb,Mo,Ti) is brittle and therefore highly undesirable as it deteriorates the mechanical properties, particularly strength and fracture toughness [9]. Wang et al. [10] reported that Laves phase represents the sites for crack initiation and propagation as well as the main nucleation site for the formation of microvoids under tensile loads. Therefore, it is crucial to eliminate the formation of Laves phase to obtain the desired microstructure and mechanical properties. The Laves phase is dissolved during homogenisation or annealing heat treatments at temperatures exceeding 954 °C in industrial practice [10–12]. Huang et al. [11] showed how different homogenisation temperatures and time influence the dissolution of the Laves phase. As reported by Cheblus et al. [12], the homogenisation temperature should be higher than 1093 °C to enable the complete dissolution of Laves phase. Wang et al. [13] reported that Laves phase cannot completely dissolve after heat treatment and that δ-phase (Ni_3Nb) precipitates at grain boundaries. Zhao et al. [14] studied the effects of different solution temperatures on δ-phase formation. The δ-phase typically forms during the annealing of PBF-LB/M IN718 parts since the annealing temperature is below δ-solvus temperature. The precipitates of δ-phase form at the grain and cellular dendrite boundaries in the shape of very small needles that provide some strengthening and prevent grain growth. However, the formation of δ-phase depletes the matrix of Nb, necessary for forming the strengthening phase [15]. During very high temperatures annealing (>1050 °C), where carbides (NbC) are thermodynamically stable and diffusion of Nb is fast enough so they can precipitate on grain boundaries and intragranular regions [16,17]. They can hinder the grain boundary sliding, leading to improved creep resistance [18].

On the other hand, the volume fraction, shape, size and distribution of Laves phase are determined by the input process parameters, such as laser power [19,20], scanning strategy [21,22], scanning speed [23,24] and laser beam diameter [25,26]. Xie et al. [15] studied the effect of the laser power and scanning speed on the solidification and formation of the Laves phase. They reported that a high cooling rate obtained at high scanning speed or low laser powers reduces the dendrite arm spacing, leading to finer and discrete Laves phase formation.

The ongoing investigation on designing the process parameters [2,27,28] and optimising heat treatments [29–31] are still carried out to customise the PBF-LB/M components in terms of microstructure and mechanical properties. The majority of studies for process parameters optimisation is based on focused beams featuring a Gaussian intensity distribution with beam diameter of 80 μm [32,33]. Although it represents a standard in the PBF-LB/M process due to the exceptional beam quality [34,35], its inefficiency, on the other hand, has been pointed out by many studies [36,37]. Focused Gaussian laser beam profile implies high-temperature gradients, instability of the melt pool as well as cooling rates, which lead to internal stresses, evaporation and spatters [38]. As a result, the appearance of microstructural defects such as pores, lack of fusion, unmelted particles and cracks from accumulated residual is increased. These defects are known stress concentrators and reduce mechanical properties of the printed parts [39,40]. These characteristics prevent the PBF-LB/M process from becoming widely useable in the industry and limit its application to small-scale production of highly specialised components, rapid prototyping, or small-series production applications.

It is therefore suggested that the change in laser beam shape and the significantly higher energy input during the PBF-LB/M process could lead to a breakthrough in AM of metallic materials, as products could be produced much faster and become more commercially attractive.

Increasing energy input typically leads to coarser microstructures with larger crystalline grains and more pronounced texture. This issue can be managed by employing different laser beam shapes and strategies, as alternative laser beam shapes provide greater flexibility in adjusting processing parameters [41,42].

Recently, significant attention has been directed toward beam shaping, an emerging technology in the PBF-LB/M process that enables the use of alternative laser intensity distributions. The Gaussian laser profile imposes limitations on achieving higher scanning speeds and increasing laser power [41], which are crucial for improving productivity. To address these constraints, researchers have begun exploring alternative laser beam shapes, such as ring-shaped profiles, which expand the process window and enhance flexibility. New laser beam profiles, such as ring-shaped intensity distributions, provide a wider process window and allow for larger beam diameters. These factors, when combined with higher laser power, can enhance productivity, reduce material waste, and minimise spatter [43]. Pérez-Ruiz et al. [44] carried out a comprehensive work where they investigated the influence of ring-shaped intensity distributions of PBF-LB/M manufactured IN718 on density, melt pool characteristics and the resulting mechanical properties. They found that beam shaping represents a helpful and promising way to tailor the microstructure and mechanical properties of the manufactured parts. In the state of the art, the most studied non-Gaussian beam profiles are ring-shaped. Therefore, it is necessary to understand the as-built microstructure for defined beam shapes and process parameters and compare it with the state-of-the-art Gaussian beam profiles and optimise the post heat-treatment.

Beam shape influences the development of microstructure in the as-printed state, but even more important is determining the optimal heat treatment temperature for a modified beam shape, as this directly affects the final mechanical properties of the product. In this respect, it is crucial to understand what happens to the microstructure when changing the laser beam shape and how it affects the mechanical properties. There is a lack of comprehensive research in the literature that connects microstructure, beam shaping, and the selection of optimal heat treatment to achieve the required mechanical properties. This study partially fills that gap by systematically investigating the influence of standard Gaussian and ring-shaped laser beam profiles on the as-built microstructure and the microstructure development. To this end, we investigated the microstructure development of Gaussian and ring-shaped beam profiles in their as-built state and after various heat treatments. Based on a comparison of mechanical properties after different heat treatments, we proposed optimal heat treatment temperatures for both Gaussian and ring-shaped beam profiles.

2. Experimental

2.1. Materials and methods

2.1.1. Material

This study utilises IN718 powder, a material recognised for its high-temperature performance, strain-age cracking and excellent weldability. The standard chemical composition of the powder ranges Ni (50–55 wt %), Cr (17–21 wt%), Nb (4.75–5.5 wt%), Mo (2.8–3.3 wt%), Ti (0.65–1.15 wt%), along with <0.2–0.8 wt% of other elements and Fe-balance [45]. According to the manufacturer EOS, the particle size distribution is between 20 and 55 μm [46]. The EDS chemical

composition of as-built samples is as follows (in wt. %): Ni 53.5 %, Cr 18.3 %, Nb 5.5 %, Mo 3.4 %, Ti 1.1 %, Al 0.8 %, Si 0.1 %, Fe 17.2 %. The difference in the chemical composition of samples produced with Gaussian and ring-shaped beam profiles is in the measurement uncertainty range.

2.1.2. PBF-LB/M machine equipped with a laser beam shaping system

PBF-LB/M system type M300 from the manufacturer EOS, equipped with a beam shaping module with a laser source capable of delivering a maximum laser power of 2 kW with a wavelength of 1050 nm, has been utilised to manufacture horizontal and vertical samples. A schematic representation of the beam shaping setup is presented in Fig. 1.

The beam shaping set up consists of a spatial light modulator (SLM) based on liquid crystal on silicon (LCOS). This system allows for precise pixel-by-pixel control of phase delays by refracting incident laser radiation through a phase mask, which is a computer-generated hologram (CGH). The laser source generates a Gaussian laser beam with a planar phase profile and a beam diameter of 80 μm. The laser beam enters the beam shaping module and is split by a beam splitter into two beams directed toward separate LCOS devices. The CGH masks are simulated based on the optical setup and desired intensity and are then applied to each LCOS. When the CGH mask is transferred to the LCOS, it induces pixel-wise tilting of the liquid crystals, resulting in local variations in the refractive index within a range of 0 to 2π. These changes influence the output laser beam profile from each LCOS in phase delay, and their superposition, combined through a beam combiner, produces the targeted intensity with the required dimensions on the building platform and focal plane.

This study employed two laser beam profiles: a standard Gaussian beam profile with a diameter of 80 μm and a ring-shaped beam profile with an outer diameter of 250 μm. Both profiles utilised pre-optimised process parameters detailed in Table 1. The dimensionless metrics, dimensionless enthalpy/dimensionless hatch distance according to Grünewald [47] are in a similar range (Table 1). The process parameters were chosen to obtain the best possible density and other built sample properties. All beam shapes were measured using a CINOGY Focus Beam Profiler 1 KF and fine-tuned using Zernike coefficients. Fig. 2 shows the beam profiles at the focal plane, while the caustic measurements for these profiles, illustrating the laser intensity distribution across a cross-sectional plane, are also presented in Fig. 2.

Vertical and horizontal cylinders are built for heat treatment optimisation and mechanical and microstructural characterisation with bidirectional hatching and a rotation angle of 67°. Details of printed cylinders and the scanning strategy are summarised in Fig. 3. A total of 48 cylinders for each laser beam profile were printed, comprising 24 horizontal cylinders and 24 vertical cylinders, to evaluate both as-built and heat-treated microstructural and mechanical properties. Prior to mechanical testing, the cylinders were machined to the geometry of tensile bar specimens in accordance with the standard ISO 6892–1:2019 [48].

The density of samples was measured by Archimedes method [49]. The results showed a high similarity between the samples produced with Gaussian and ring-shaped beam profiles, with densities of 99.90 % and 99.85 %, respectively, relative to the reference density of 8.24 g/cm^3.

2.1.3. Heat treatment

Heat treatment of as-built cylindrical blocks (ϕ11 mm × 80 mm) was performed in a high-pressure horizontal vacuum furnace TAV H2–S. Vacuum heat treatment included 1 h of solution annealing, followed by two steep aging (718 °C/8 h and 621 °C/9 h). Specimens were first heated to the solution annealing temperature using a 25 °C/min heating rate and two equalising steps at 650 °C and 850 °C. Four different solution annealing temperatures were used, namely 954 °C, 984 °C, 1034 °C and 1154 °C, respectively. After 1 h solution annealing, all specimen groups were fast cooled by nitrogen gas (1 bar, 1.5 °C/s) to about 700 °C, reheated to 718 °C and aged for 8 h, then slowly cooled with furnace (3.5 °C/min) to 621 °C and further aged for 9 h, with final cooling to room temperature in nitrogen gas at 1 bar (1.5 °C/s). The heat treatment diagram for the solution annealing temperature of 954 °C is shown in Fig. 4.

2.1.4. Microstructure characterisation

Metallographic samples were prepared by embedding them in conductive Bakelite resin, followed by sequential grinding and polishing with 3 μm and 1 μm diamond paste for 15 min, respectively. Light microscopy (LM) was carried out to understand melt-pool shapes and dendrite growth using a Carl Zeiss AXIO Imager.Z2m. The samples were etched with 10 ml HNO_3, 10 ml acetic acid (CH_3COOH), 15 ml HCl and 2–5 drops of glycerol ($C_3H_8O_3$).

For microstructure and fracture analysis, scanning electron microscopy (SEM) equipped with a backscattered electron detector was utilised. The metallographic preparation was the same as for LM with an additional final 30 min colloidal silica nanoparticles (OPS) polishing. The same polishing procedure was applied for electron backscatter diffraction (EBSD) analysis. For EBSD analyses we used a Zeiss CrossBeam 550 FIB SEM system, which was integrated with an EDAX Hikari Super EBSD camera and EDAX APEX software. Additionally, the setup included an EDAX Octane Elite EDS detector. Postprocessing with EDAX OIM software using spherical indexing techniques was performed to achieve optimal results from the EBSD analysis. This configuration enabled detailed characterisation through secondary electron (SE) imaging, energy-dispersive X-ray spectroscopy (EDS), and electron backscatter diffraction (EBSD), allowing us to gather both compositional and crystallographic data. Analytical parameters were carefully optimised, with SE, backscattered electron (BSE), and EDS mapping analyses conducted at a 15 kV accelerating voltage and a probe current of 2.0–5.0 nA. In contrast, EBSD required a probe current of 10.0 nA and a sample tilt 70°.

The SEM BSI particle analysis was conducted on two samples, which were manufactured using Gaussian and ring-shaped beam profiles and

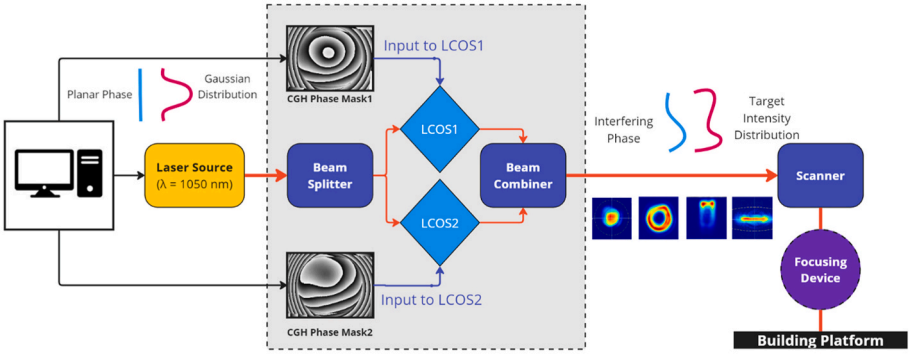

Fig. 1. Schematic illustration of the PBF-LB/M system from EOS type M300 equipped with beam shaping module [46].

Table 1
Process parameters used for manufacturing testing specimens.

	Laser power (W)	Layer thickness (μm)	Beam diameter (μm)	Volume energy density (J/mm^3)	Build rate (mm^3/s)	Dimensionless enthalpy $\Delta H/h_s$	Dimensionless enthalpy/hatch distance $(\Delta H/h_s)/h^*$
Gaussian beam profile	360	80	80	39.1	9.2	17.22	8.33
Ring-shaped beam profile	700	80	250	54.7	12.8	5.22	7.29

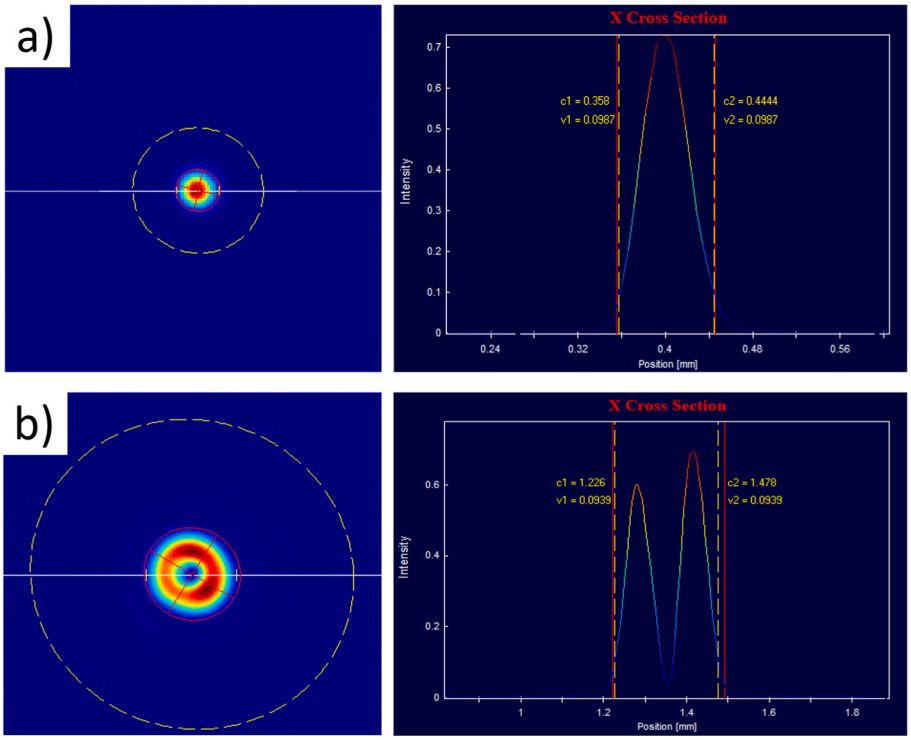

Fig. 2. a) Caustic measurement of the Gaussian beam profile with a diameter of 80 μm and b) ring-shaped beam profile with an outer diameter of 250 μm. The laser intensity distribution across the diagonal cross-section of the laser beam is displayed in the right-side images.

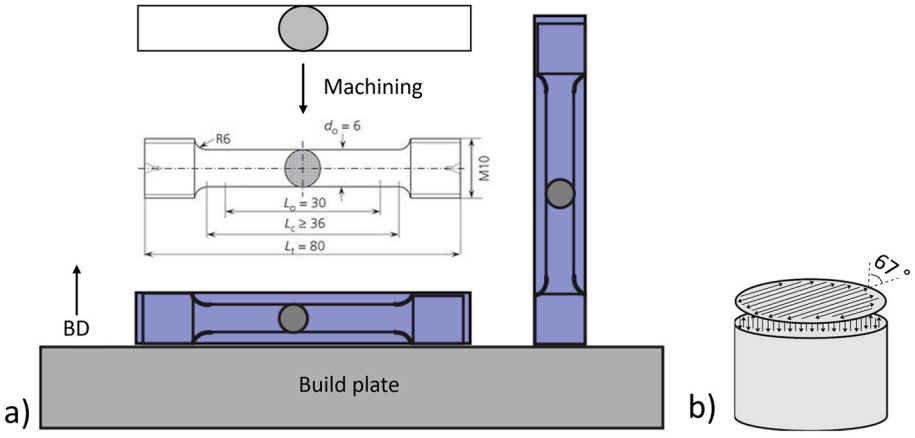

Fig. 3. a) Sketch of the position of cylindrical blocks on build plate from which standard tensile bar specimens were machined (BD – build direction) and b) sketch of laser beam path showing rotation angle 67° at the next layer.

subsequently heat-treated at a temperature of 1154 °C. The analysed surface area for both samples was identical at 5.71 mm^2. The particle analysis used grey-intensity threshold analysis, defining brightness levels and a minimum particle size of 0.2 μm. Additionally, the composition of smaller phases was examined using EDS in a scanning electron microscope. (Scanning) Transmission electron microscopy ((S) TEM) analysis was performed in a TEM/STEM Thermo Fisher Scientific Talos f200i equipped with Thermo Fisher Scientific Super-X 4 × 30 mm^2 objective pole piece. TEM lamellas were prepared in ZEISS Crossbeam 550 FIB-SEM Gemini II using Ga ions.

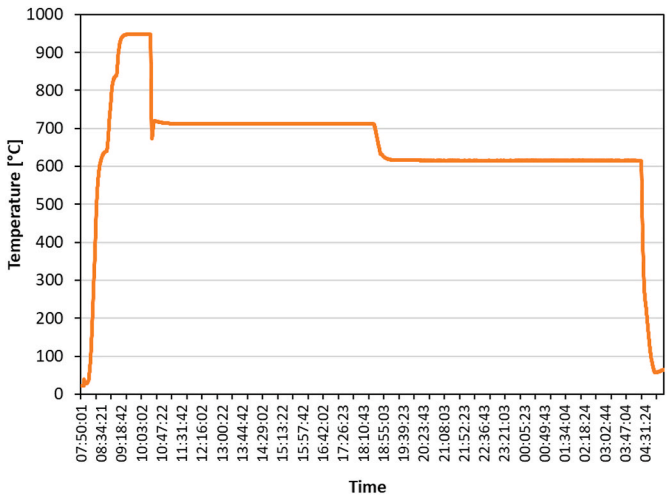

Fig. 4. The heat treatment temperature profile shows solution annealing and two-stapes ageing.

2.1.5. Mechanical analysis

From as-built and heat-treated cylindrical blocks, standard tensile bar specimens (type B, ϕ 6 mm × 30 mm; Fig. 3) were machined and tested at room temperature according to standard ISO 6892–1:2019 [48], using the A224 testing method. Yield strength, ultimate tensile strength and elongation at fracture were determined for each specimen and average values were calculated.

Hardness test measurements were performed on Vickers hardness tester Falcon 800GZ according to EN ISO 6507–1:2023 standard [50].

3. Results

3.1. Microstructure characterisation

Different volumetric energy inputs and beam shapes of the PBF-LB/M process are responsible for the different shapes of melt pools, the varying temperature distribution in the solidification zone, and the solidification rate and subsequent thermal effects of the laser. All of this influences the development of microstructure and the frequency of epitaxial growth between dendritic grains across melt pools. Fig. 5 shows the microstructure of as-built samples obtained using two different beam shapes during the PBF-LB/M process. The etched metallographic sample reveals traces of melt pools with narrow and deep shapes for the Gaussian beam profile. Dendrites are randomly distributed, with no directional growth, extending from the centre in all directions (Fig. 5a). In the case of the ring-shaped beam profile, the melt pools are broader and shallower, with dendrites predominantly following the growth direction along the build direction (Fig. 5b). Similar dendrite growth directions can be observed in BE images (Fig. 5c and d). Images at higher magnifications reveal the typical γ matrix structure of a Ni-based alloy described as a dendritic structure composed of sub-dendrites. Inside sub-dendrites, the dislocation cells are present

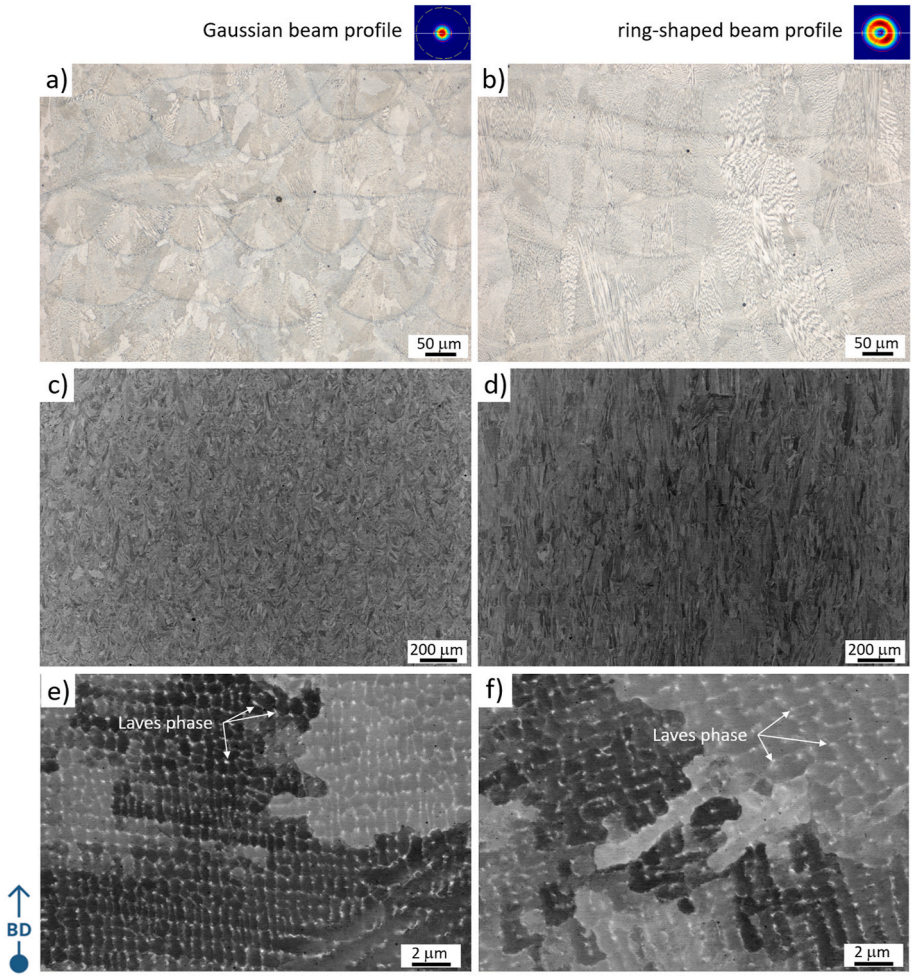

Fig. 5. Microstructures obtained by Gaussian (left) and ring-shaped beam profile (right) in build direction; a), b) light microscopy images of etched samples, c), d) BE images of polished samples at lower and e), f) higher magnifications.

what is usually described as cellular structure [51,52]. Due to the broader ring laser beam shape and higher energy input, the solidification rate is reduced, resulting in larger dislocation cells [53] compared to those formed at the Gaussian beam profile (Fig. 5e and f). Nb and Mo segregation at the cell boundaries [8] is responsible for the Laves phase formation in the microstructure. The estimated volume fraction of the Laves phase for both samples is very similar and does not differ significantly. When estimating the size, it is important to consider that the cells are cut transversely; only in this way, accurate values can be obtained. Due to the larger cellular structure obtained by the ring-shaped beam profile, we estimate that the individual Laves phases are also slightly larger. However, after observing several areas, we undoubtedly estimate that the size of the dendritic cells is at least 30 % larger for the ring-shaped beam profile.

Fig. 6 shows the microstructure development after different post-heat treatments as well as the microstructure in the as-built state for both investigated laser beam shapes. Heat treatment at a temperature of 954 °C causes the dissolution of the Laves phase and the precipitation of δ-phase in the same regions. Cellular borders are rich in Nb and Mo, which leads to the precipitation of δ-phase in the form of needles along dendrites, sub-dendrites and cell structure boundaries, similarly for both laser beam shapes. Larger and shallower melt pools obtained by the ring-shaped beam profile cause larger cells, sub-dendrites and dendrites, which represent the main difference in the microstructure between both

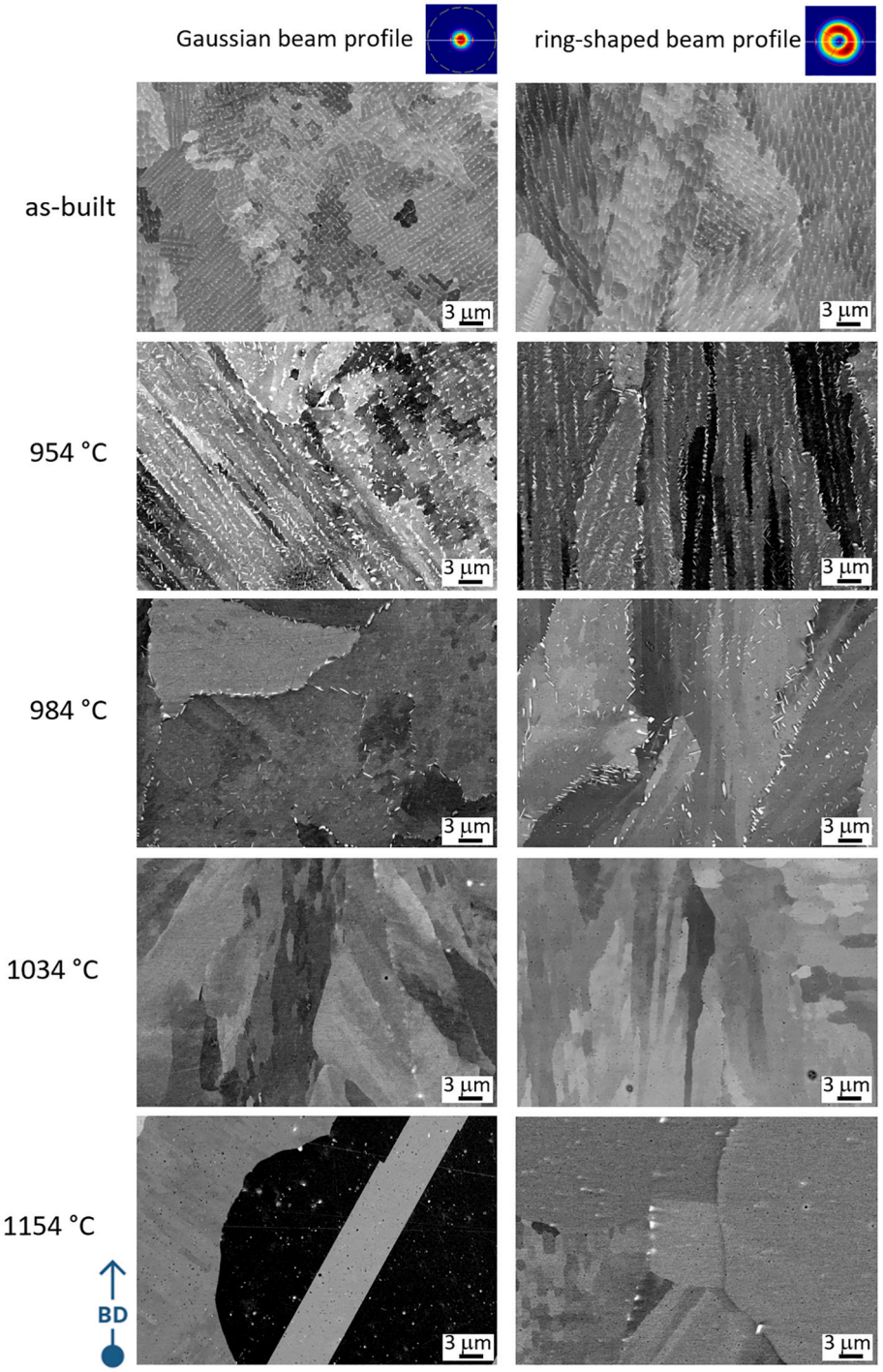

Fig. 6. BE images of as-built and post-heat-treated samples produced by Gaussian (left) and ring-shaped beam profile (right).

beam shapes. When the heat treatment temperature is increased by 30 °C–984 °C, the number of δ-phase precipitates in the microstructure decreases. The needles of the δ-phase are located along the dendrite and sub-dendrite boundaries, very similar for both investigated laser beam shapes. Further increase of the heat treatment temperature to 1034 °C additionally reduces the amount of precipitated δ-phase, which is almost completely absent for both laser beam shapes. However, a heat treatment at a temperature of 1154 °C causes recrystallisation and grain growth. Bright, angular MC carbides appear in the microstructure [54]. The carbides form in rows, likely along the previous dendritic boundaries rich in Nb. In both cases, for Gaussian and ring-shaped beam profiles, there are areas where recrystallisation did not occur or a substructure is visible within the grains. This is because there was insufficient energy or stress in the material for recrystallisation.

In addition to microstructural changes, we also examined the shape and size of crystalline grains in the as-built state and after heat treatment (Fig. 7). The sample produced with the Gaussian laser beam profile has a fine-grained structure with an average grain size of 36.5 μm^2. The grain shape is typical for the PBF-LB/M process in the build direction, where the shape of the melt pool is somewhat noticeable. However, because epitaxial growth occasionally occurs between the melt pools in the subsequent layer, the grain shape does not entirely follow the melt pool [55]. The orientation of the crystalline grains is almost ideally random. On the other hand, the sample produced with the ring-shaped beam profile exhibits a distinctly columnar crystal structure in the build direction. The grains are much larger, with an average size of 106.3 μm^2. Additionally, a fairly intense texture is already visible in the EBSD images. During heat treatment of up to 1034 °C, no recrystallisation occurs for the Gaussian or ring-shaped beam profile samples. At a heat treatment temperature of 1154 °C, recrystallisation and grain growth occur in both samples, regardless of the laser beam profile (Gaussian or ring). However, upon recrystallisation, the sample made with the Gaussian laser beam profile has smaller recrystallised grains than the one made with the ring-shaped beam profile, with an average area of 119.9 μm^2. In contrast, the sample made with the ring-shaped beam profile has an average area of 181.9 μm^2. Despite recrystallisation, the crystalline grains are slightly elongated in the build direction, which is more characteristic of the ring-shaped beam profile sample. Even though the EBSD images suggest complete recrystallisation, the BE image (Fig. 6) reveals areas where recrystallisation did not occur or where substructures are still visible within the recrystallised regions, valid for both laser beam shapes.

Fig. 8 shows the Pole Figures (001) of as-built and heat-treated (at 1154 °C) samples produced with Gaussian and ring-shaped beam profiles. The sample produced with the Gaussian beam profile has almost no texture, with a texture intensity of 1.3, while the sample produced with the ring-shaped beam profile has a pronounced texture, with a texture intensity of 7.4. The texture components (100)[001] and (110)[001] are quite prominent. After the recrystallisation of the sample produced with a Gaussian beam profile, grain growth and a slight texture strengthening occur; however, the texture intensity is only 2.5. Recrystallisation results in significant grain growth and a decrease in texture intensity to 3.2 in the ring-shaped beam profile produced sample. Due to the strong initial texture, the sample retains a somewhat pronounced texture even after recrystallisation. This is also because the grains are extremely large.

To observe how the substructure changes, further EBSD data analysis offers greater insight into the alterations in grain substructure resulting from heat treatment. The Grain Average Misorientation (GAM) of parts produced by Gaussian and ring-shaped beam profiles, and heat-treated at 1034 °C and 1154 °C, exhibited some differences (Fig. 9). The main difference is that the part produced by the Gaussian beam profile and heat-treated at 1034 °C contains a greater number of grains with a GAM range between 1.0° and 5.0° in comparison to the ring beam profile (Table 2). This indicates that there is a larger amount of substructure present, along with significant orientation changes in part produced by the Gaussian beam profile. Such a structure demonstrates a stronger driving force for recrystallisation. This is reflected in GAM distribution when samples are heat treated at 1154 °C, where the opposite is observed. Part produced by the ring-shaped beam profile and heat treated at 1154 °C has more grains with a GAM range between 0.5° and 5.0° compared to the Gaussian beam profile. The blue fraction with GAM values of 0.0° and 0.5° consists of fully recrystallised grains. Consequently, a fraction of recrystallised grains is primarily generated by the Gaussian beam profile and heat treated at 1154 °C.

SEM/EDS mapping was conducted to assess the volume fraction and types of carbide phases in samples fabricated using both laser beam shapes. Automated SEM particle analysis revealed differences in the proportion of MC carbides over a larger area between the two sample types. In a 0.71 mm^2 area, samples produced with the Gaussian beam profile contained 1125 carbide particles, whereas those produced with the ring laser beam shape had 946 particles. The average particle sizes were similar: 0.77 μm for the Gaussian and 0.76 μm for the ring-shaped beam profile. The total carbide particles surface area in the measured region was 879.5 μm^2 for the Gaussian beam profile and 731.0 μm^2 for the ring-shaped beam profile. Thus, the carbide phase's number and surface area were 20 % smaller in samples produced with the ring-shaped beam profile. Fig. 10 presents the microchemical map analysis of both samples at low magnification, illustrating the distribution of MC carbides and at higher magnification, confirming that these phases are rich in Nb, Ti, C, and N. Additionally, a point analysis was conducted on one of the larger carbides for both types of samples. The distribution of Nb and Ti, displayed in EDS maps (Fig. 10a–c), indicates that MC carbides precipitate along prior high-angle dendritic boundaries. Some carbide chains are also observed at the boundaries of recrystallised grains. It is known that precipitates formed during heat treatment inhibit further grain boundary movement. Based on EDS mapping and point analysis (Fig. 10b–d), it can be assumed that the precipitates formed are carbonitrides of the MX type (M = Nb, Ti; X = C, N). Although EDS analysis of light elements is not highly precise, the observed atomic ratio of M is approximately 1, which supports our assumptions and aligns with literature data [54]. The image of the carbide's distribution for the ring laser beam shape sample indicates a slightly lower quantity, yet they are similarly arranged along prior high-angle dendritic boundaries.

The literature [16,56] suggests that some carbides form already during the printing process, while some authors report that the solvus temperature of MC carbides ranges between 1040 °C and 1200 °C [54]. The carbides that form during printing are embedded within the Laves phases, as these regions are rich in Nb, making them difficult to detect in SEM images. During heat treatment, the Laves phase dissolves, revealing the carbides in these areas, as shown in Fig. 11a and b. At higher heat treatment temperatures, recrystallisation occurs, leading to the growth of existing carbides or the formation of new ones. Fig. 11c, d illustrate that, compared to lower heat treatment temperatures, the number and size of carbides increase significantly. Additionally, previous automatic EDS analysis confirmed that carbide proportions are higher in samples produced with the Gaussian beam profile.

During the ageing process, γ' and γ'' precipitates form and play a critical role in the precipitation strengthening of IN718. Consequently, it is essential to characterise these phases and evaluate whether laser beam shape has any influence on their size, spatial distribution, or volume fraction. Fig. 12 displays Bright-Field Scanning Transmission Electron Microscopy (BF–S) and High-Angle Annular Dark Field (HAADF) images of specimens produced using Gaussian and ring-shaped laser beam profiles. Both samples were heat-treated at 1034 °C and then aged. A comparative analysis of the micrographs indicates no significant differences in the morphology, distribution, or amount of γ'/γ'' precipitates between the two processing conditions. A broader survey of the microstructure confirmed the absence of notable variations.

The γ' and γ'' precipitates exhibit distinct differences in both morphology and chemical composition. The γ' phase generally appears

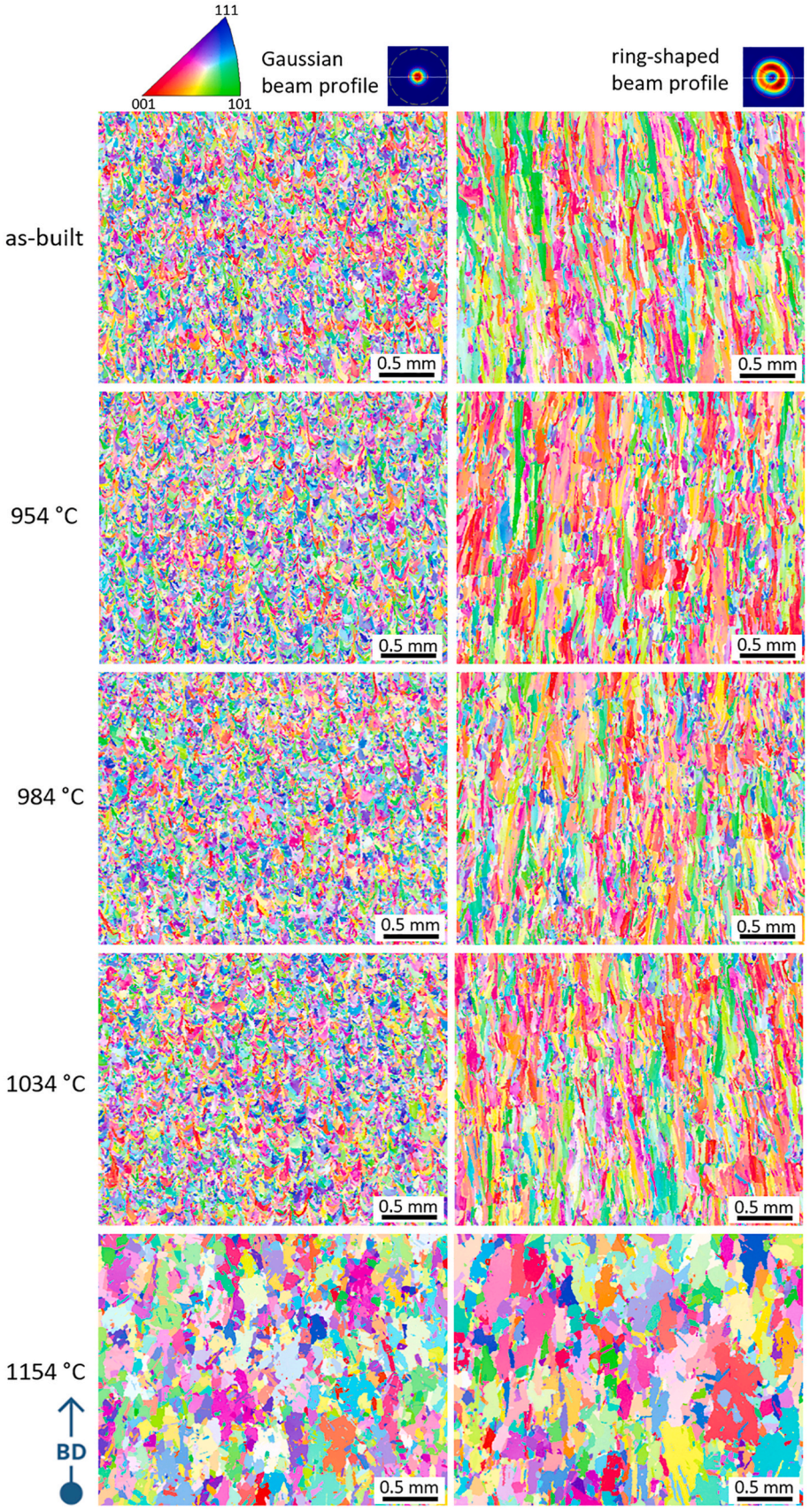

Fig. 7. EBSD IPF Z cross-sections in the building direction of as-built and post-heat-treated samples produced by Gaussian (left) and ring-shaped beam profiles (right).

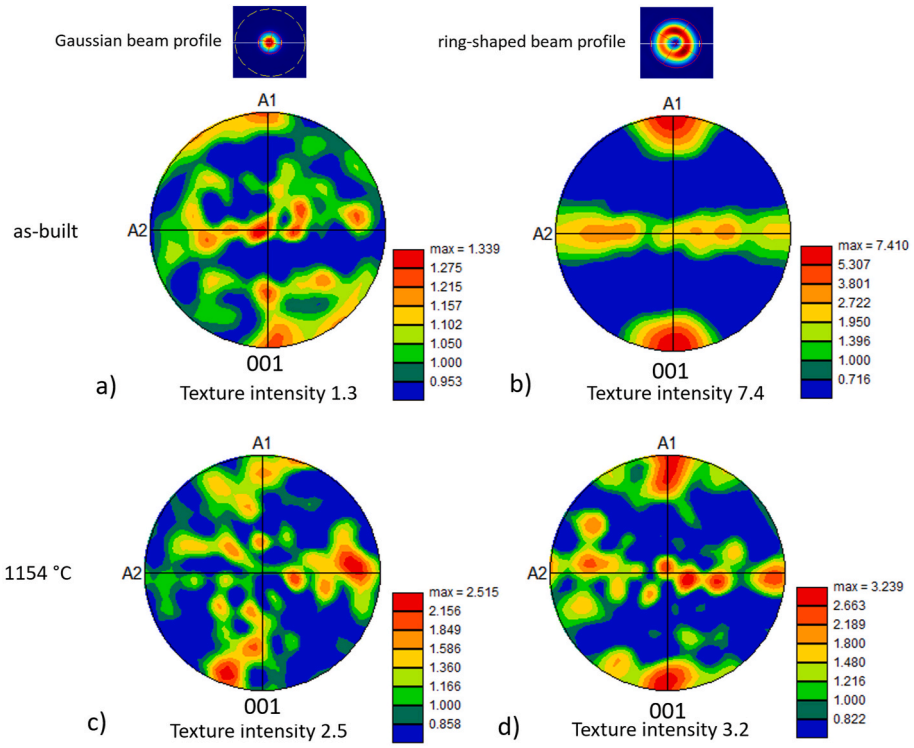

Fig. 8. (001) Pole figures of as-built and post-heat-treated (at a temperature of 1154 °C) samples produced by Gaussian (left) and ring-shaped beam profiles (right).

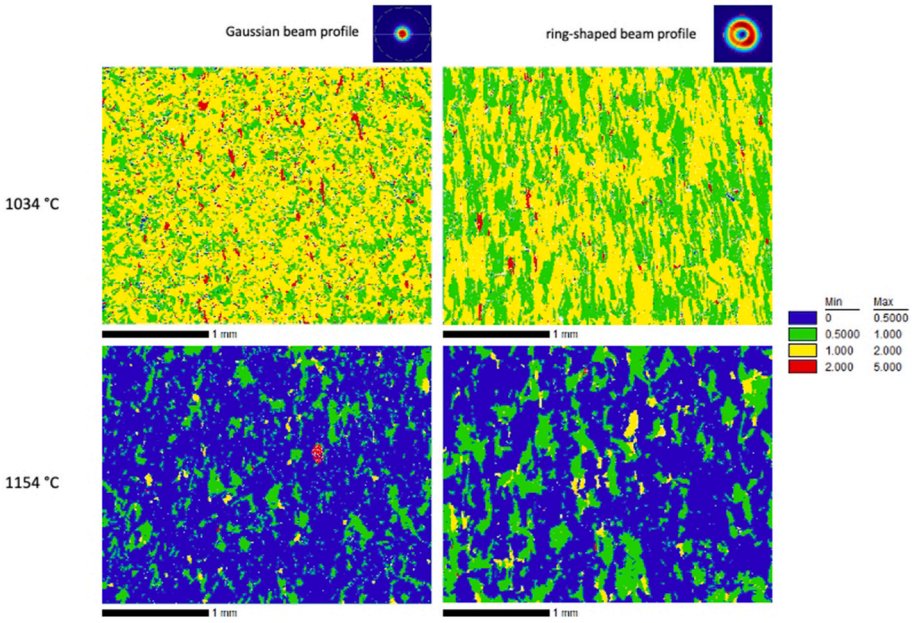

Fig. 9. GAM image of post-heat-treated samples at 1034 °C and 1154 °C, produced by Gaussian (left) and ring-shaped beam profiles (right).

Table 2
Fraction of grains with different GAM ranges for parts produced by Gaussian and ring-shaped beam profiles and heat treated at 1034 °C and 1154 °C.

Misorientation angle		Gaussian beam profile		Ring-shaped beam profile	
Min.	Max.	1034 °C	1154 °C	1034 °C	1154 °C
0°	0.5°	0.016	0.814	0.004	0.711
0.5°	1.0°	0.238	0.164	0.397	0.248
1.0°	2.0°	0.687	0.016	0.546	0.0370
2.0°	5.0°	0.038	0.002	0.013	0.001

as spheroidal or rounded particles, whereas γ″ tends to form elongated, needle-like structures. Chemically, γ′ corresponds to $Ni_3(Al,Ti)$, while γ″ is identified as Ni_3Nb [2]. Distinguishing these phases based solely on morphology is inherently limited due to the projection nature of TEM imaging, which may obscure true three-dimensional geometry. Therefore, compositional analysis was carried out using TEM coupled with EDS. Precipitates enriched in Al and Ti were attributed to the γ′ phase, while Nb-enriched regions were classified as γ″. Nickel was detected in both types of precipitates, as expected from their nominal compositions. Fig. 13 shows EDS elemental maps of samples produced with the

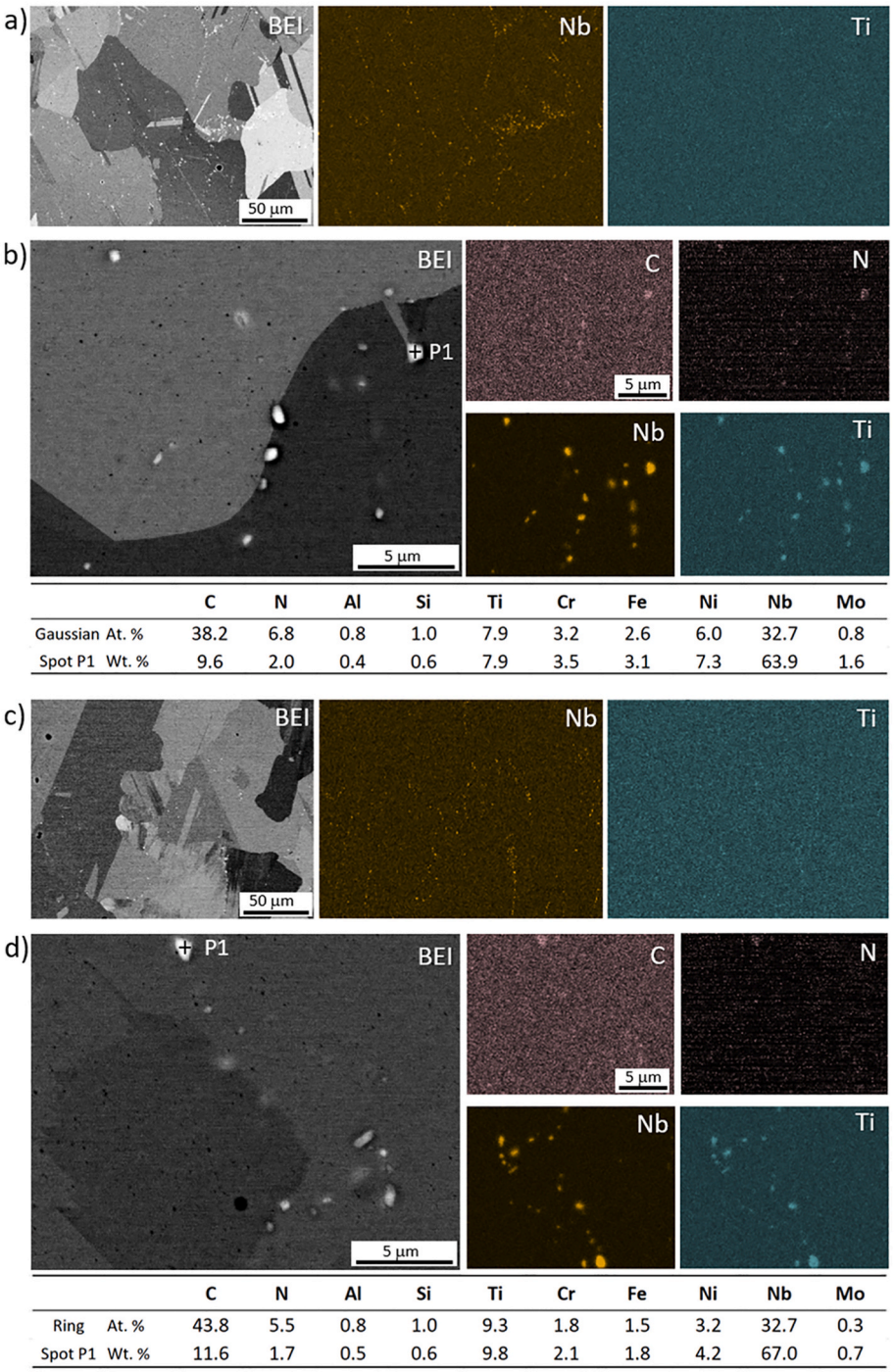

		C	N	Al	Si	Ti	Cr	Fe	Ni	Nb	Mo
Gaussian	At. %	38.2	6.8	0.8	1.0	7.9	3.2	2.6	6.0	32.7	0.8
Spot P1	Wt. %	9.6	2.0	0.4	0.6	7.9	3.5	3.1	7.3	63.9	1.6

		C	N	Al	Si	Ti	Cr	Fe	Ni	Nb	Mo
Ring	At. %	43.8	5.5	0.8	1.0	9.3	1.8	1.5	3.2	32.7	0.3
Spot P1	Wt. %	11.6	1.7	0.5	0.6	9.8	2.1	1.8	4.2	67.0	0.7

Fig. 10. SEM/EDS analyses of Gaussian sample (a, b) and ring-shaped beam profile samples (c, d); a), c) BE images with corresponding Nb and Ti maps, b), d) BE images with marked spot analysis, and corresponding C, N, Nb and Ti maps with microchemical composition for one of the carbonitride phases.

Gaussian and ring beam profiles. EDS elemental maps did not show significant differences in the amount and share of γ′ and γ″ precipitates between both beam profiles.

Given the very small size of the precipitates, we additionally performed a line-scan EDS analysis to correlate their morphology with the three key elements that constitute the γ′ and γ″ phases. As shown in Fig. 14, regions exhibiting elevated concentrations of Al and Ti are associated with a reduced Nb content. In the micrographs, these regions correspond to spherical precipitates, which are characteristic of the γ′ phase, whereas areas with higher Nb and lower Al and Ti concentrations correspond to needle-like precipitates, typically associated with the γ″ phase. As previously noted, no significant differences were observed in the surface density of either type of precipitate across the analysed samples for both beam shapes.

3.2. Mechanical properties

Fig. 15 shows the results of the tensile tests: the average yield and the ultimate tensile strength, the elongation as well as contraction of samples produced in the horizontal and vertical directions by Gaussian and ring-shaped beam profiles, in as-built state and post-heat-treated at different temperatures. The as-built state shows considerably lower

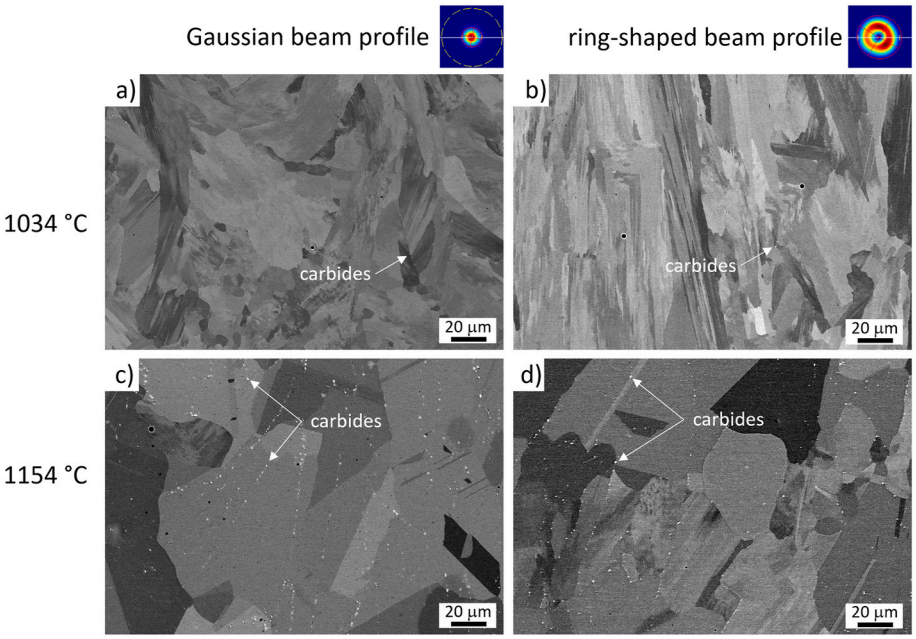

Fig. 11. BE-images of heat-treated samples at 1034 °C (a, b) and 1154 °C (c, d) produced by Gaussian (left) and ring-shaped beam profile (right).

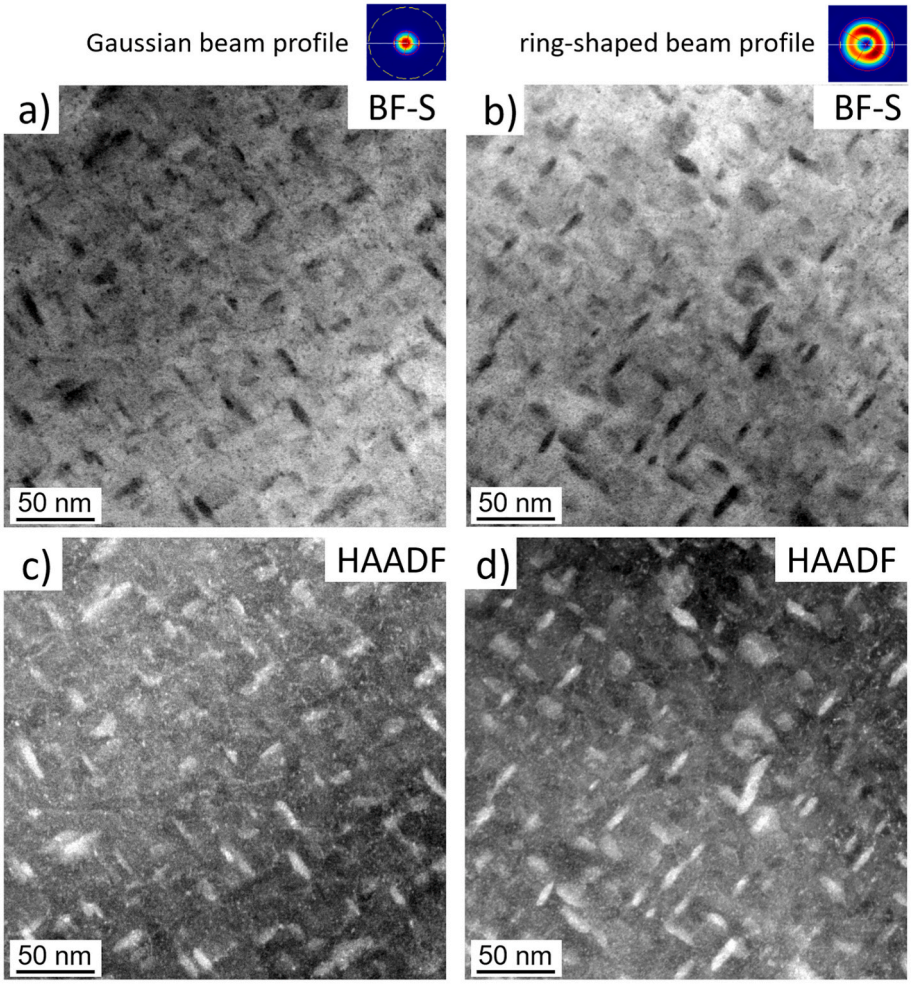

Fig. 12. TEM images of γ′ and γ″ precipitates produced with (a, c) Gaussian beam profile and (b, d) ring beam profile.

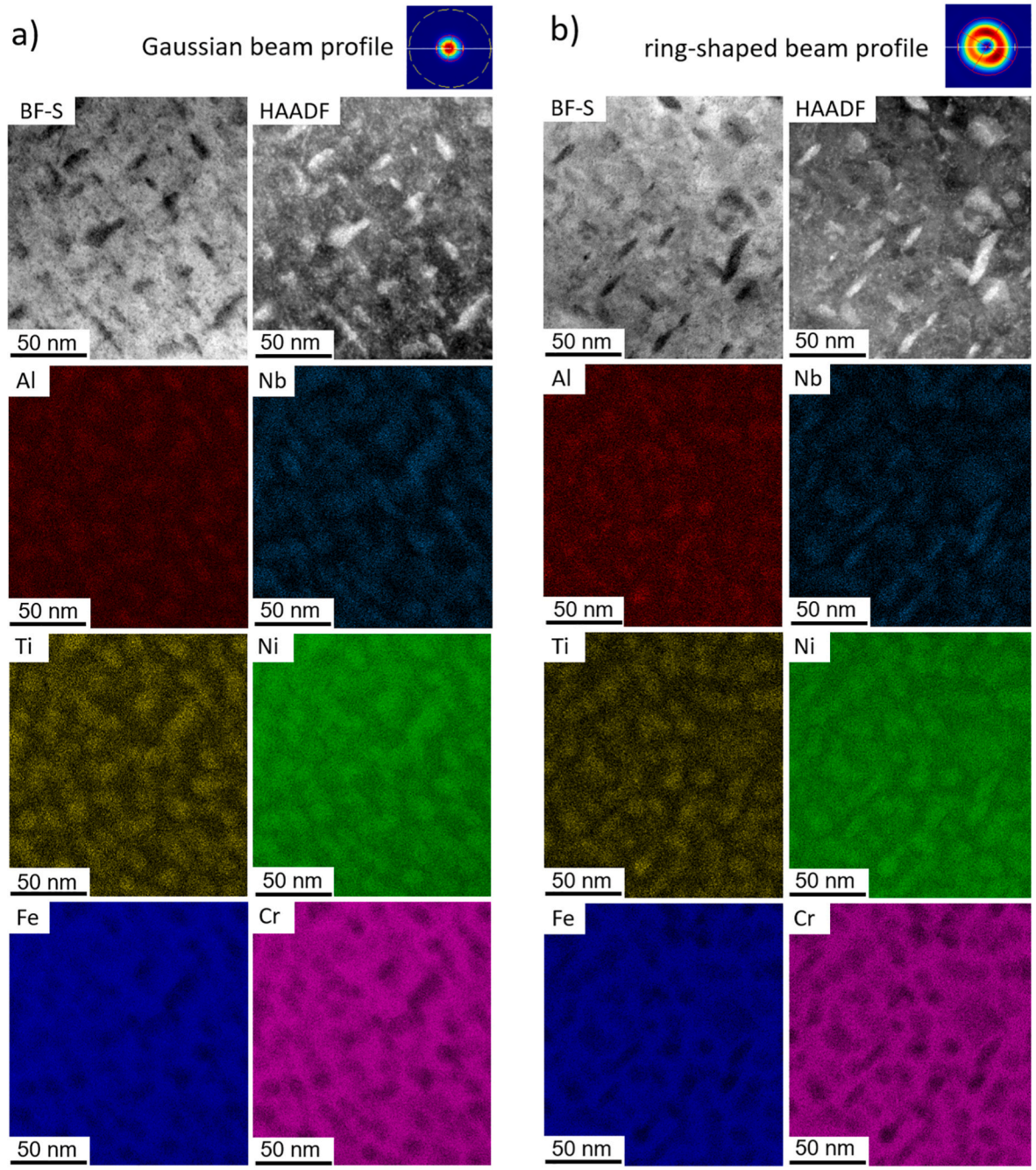

Fig. 13. TEM/EDS maps of samples produced with a) Gaussian beam profile and b) ring beam profile.

average yield and ultimate tensile strength on account of not being post-heat treated (Fig. 15a and b). The samples produced with Gaussian beam profile exhibit a bit larger value of ultimate tensile strength and yield strength in both directions, however, the samples produced with ring-shaped beam profiles have more isotropic properties.

After all post-heat treatment temperatures, the mechanical properties of all samples are significantly increased. However, samples produced with the ring-shaped beam profile exhibit an average 3–7 % reduction in yield and ultimate tensile strength compared to those produced with the Gaussian beam profile. A notable difference in strength between horizontally and vertically built samples subjected to heat treatment at 954 °C was observed when comparing samples produced with the Gaussian and ring-shaped beam profiles. Samples created with the Gaussian beam profile displayed larger differences in yield and ultimate tensile strength between horizontal and vertical build directions (7.9 % and 9.5 %, respectively) compared to those made with the ring-shaped beam profile (3.7 % and 3.1 %, respectively). At higher heat treatment temperatures (984 °C), these differences between horizontal and vertical samples decreased for both laser beam shapes (to approximately 2 %). The yield strength of samples produced with Gaussian and ring-shaped beam profiles increases with annealing temperatures up to 1034 °C, while ultimate tensile strength remains similar (984 °C) or decreases at 1034 °C. Heat treatment at 1154 °C significantly lowers both yield and ultimate tensile strength. Further, the samples in the as-built state show much higher average elongation and contraction than the heat-treated samples (Fig. 15c and d). This is a well-known phenomenon for precipitation-hardened alloys. Samples built horizontally using the ring-shaped beam profile exhibit higher average elongation and contraction compared to vertically built samples. These differences in elongation and contraction between horizontal and

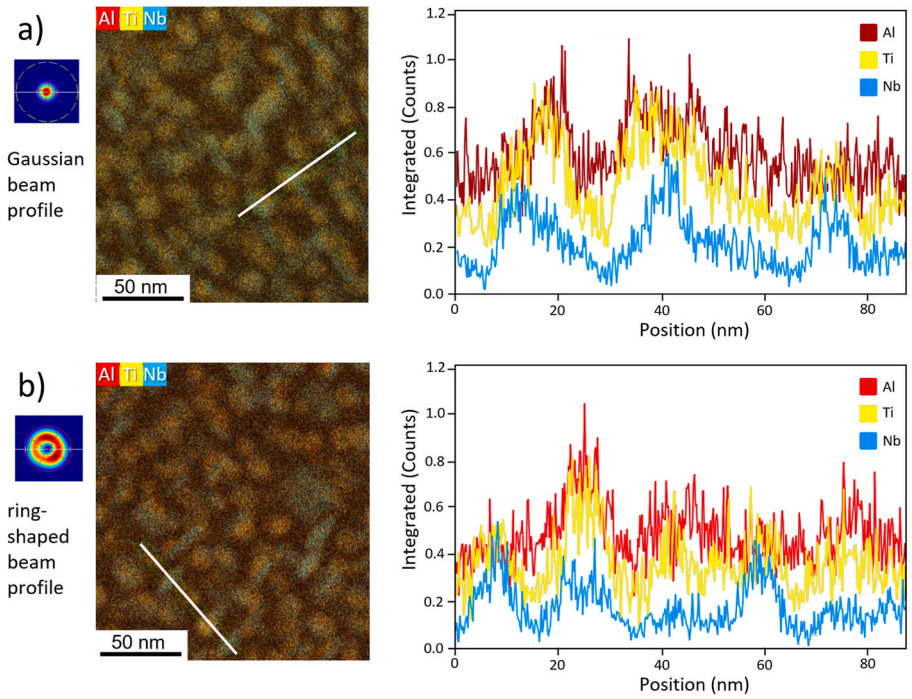

Fig. 14. TEM/EDS line scan (marked with white line on composite EDS maps of three elements) of precipitates in the samples produced with a) Gaussian beam profile and b) ring beam profile.

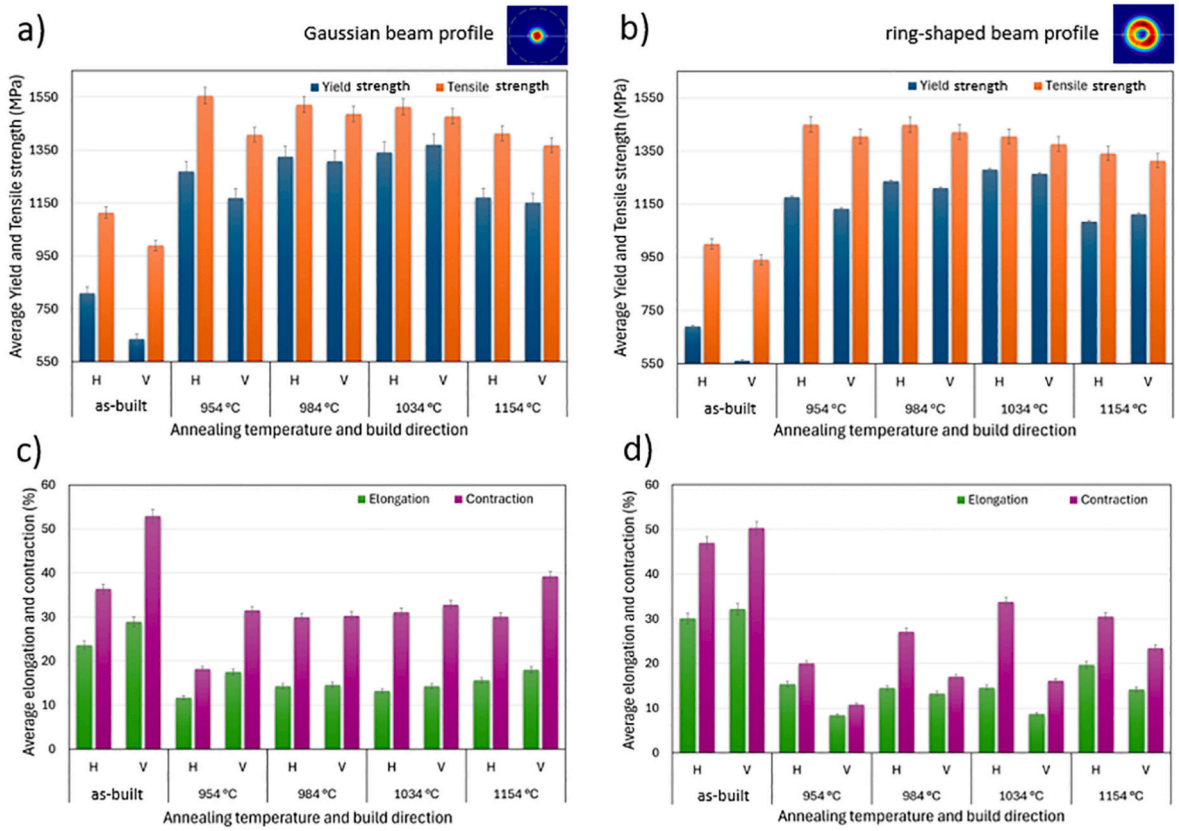

Fig. 15. Mechanical analysis performed at room temperature of samples processed with Gaussian and ring-shaped beam profiles in their as-built and different post heat-treated conditions; a) average yield and tensile strength of Gaussian and b) ring-shaped beam profiles, c) average elongation and contraction of Gaussian and d) ring-shaped beam profiles.

vertical samples persist even at the highest annealing temperature of 1154 °C. In contrast, this effect is not observed in samples produced with a Gaussian beam profile. Large differences in elongation and contraction values for horizontal and vertical samples exist only in samples heat-treated at 954 °C and 1154 °C. In two examples (954 °C and 1034 °C, Fig. 15d), the elongation of vertical samples built by ring-shaped beam profile is very low (about 8.4–8.7 %).

Additionally, the fracture surfaces were investigated, and several lacks of fusion pores were found in these samples, although fracture surfaces of the Gaussian beam profile exhibited slightly fewer pores (Fig. 16). Fig. 16 a, b show the low magnification fracture area and a fracture detail in the insets. Fig. 16c highlights the presence of pores in the fracture area of the sample produced with a ring-shaped beam profile, explaining the low elongation and contraction values of this sample. It is well known that pores in the vertical direction have a more significant impact on elongation and contraction than in the horizontal direction, as shown in the diagram in Fig. 15. Since all vertical samples produced by ring-shaped beam profile show lower average elongation values than horizontal samples, we can assume that most samples contain a lack of fusion pores (Fig. 15c).

Vickers hardness measurements present in Fig. 17 show hardness in as-built state and after heat treatment for both beam shapes. Considering that IN718 achieves its final mechanical properties and hardness through precipitation hardening, it is evident that the hardness in the as-built state is lower than after heat treatments, despite the fact that additively manufactured materials possess a dislocation cell structure that significantly strengthens the material. In general, samples produced with a ring-shaped beam profile exhibit slightly lower hardness; however, at a heat treatment temperature of 1034 °C, both hardness values become fairly comparable.

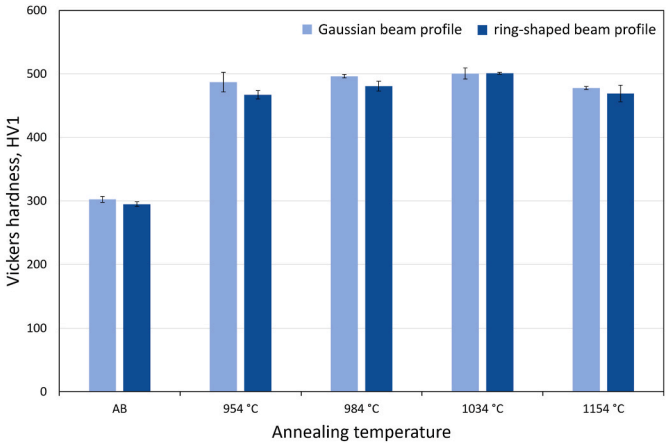

Fig. 17. Vickers hardness measurements of samples produced by Gaussian and ring-shaped beam profiles in their as-built (AB) and different post-heat-treated conditions.

4. Discussion

The size and orientation of the dendrites, sub-dendrites, and cell structures in the PBF-LB/M-processed metallic material depend on the process parameters, primarily the cooling rate and the temperature gradient, defined by the laser beam profile. In our case, the main difference is the shape of the beam, different input energy (Table 1), and beam energy intensity distribution (Fig. 2). Due to different beam profiles and, thus, different volumes of melt pools, different input energy is needed to enable melting with comparable enthalpy. The ring beam shape produces a melt pool with a lower depth-to-width ratio [41,57] than the Gaussian beam profile (Fig. 2a and b). With the Gaussian beam profile, a more significant percentage of the columnar grains grow declined to the building direction, especially at the edges of the melt pool. At the melt pool edges, grains grow in the direction of the highest thermal gradient, which is typically expected to the edge of the melt pool [58]. The preferential growth of fcc metals is parallel to (100).

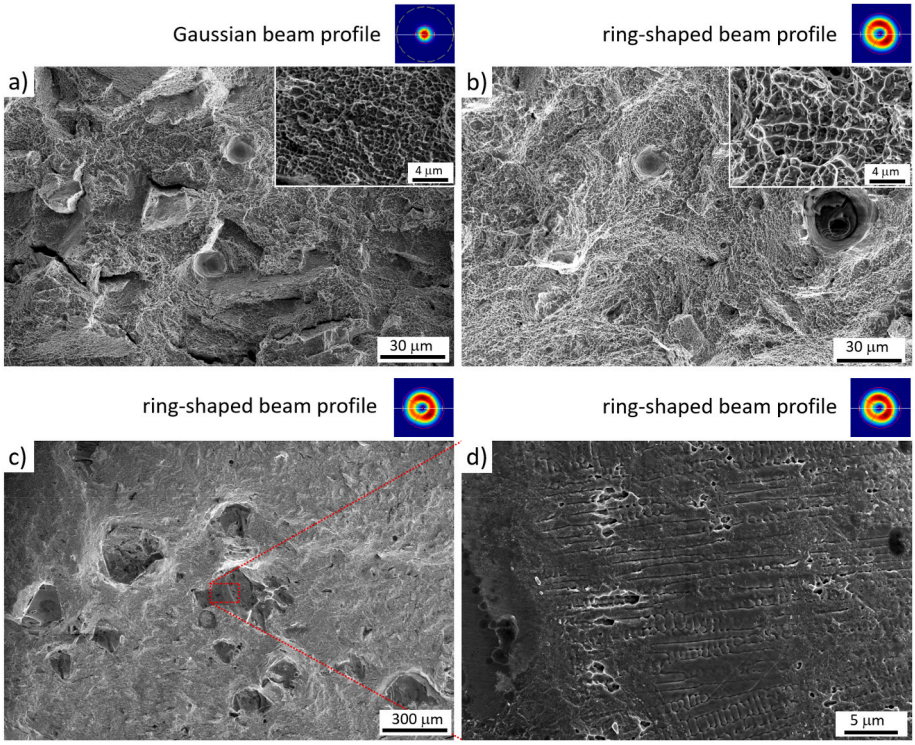

Fig. 16. Fracture surface images obtained by the SE detector, a) Fracture surface of the tensile test sample produced with a) Gaussian and b) ring-shaped beam profiles, with an enlarged detail in the upper right corner showing dendrite size, c) lower magnification of the fracture surface of the tensile test sample produced with ring-shaped beam profile, showing a pore cluster, and d) detail showing the dendritic surface in the pore.

Thus, the Pole figure texture for (001) has lower intensity, especially in the build direction (Fig. 8a). The opposite happens for a ring-shaped beam profile where a melt-pool edge has a lower curvature (Fig. 2b). Furthermore, the ring-shaped beam profile does not have the highest intensity in the middle but on the beam's edges. Because of this, the highest thermal gradient is oriented along the building direction. Therefore, the conditions are fulfilled in the middle and on the edges of the melt pool so that columnar grains can grow in the building direction. Thus, the texture intensity for parts made by the ring beam is very high, especially in the building direction (Fig. 8a). In the as-built state, dendrites, sub-dendrites, and dislocation cells are larger in the sample produced with a ring-shaped beam profile. This difference persists during heat treatment. Dislocation cells begin to disappear; however, some remain between 800 and 900 °C. Above this temperature, the remaining dislocation cells transform into substructures within recrystallised grains [59]. Dendrites, or grains, remain stable until the recrystallisation temperature, which occurs above 1050 °C [60]. Based on the results of tensile tests and hardness measurements, it is evident that these structures (dendrites, sub-dendrites, and cells) influence mechanical properties. Since the sizes of these structures are larger in the ring laser beam shape sample, this sample exhibits slightly inferior mechanical properties. Interestingly, at a heat treatment temperature of 1034 °C, the hardness values of both types of samples equalise despite the differences in grain size and substructure between parts produced by Gaussian and ring-shaped beams (Fig. 9). This demonstrates that the role of grain size and substructure is less critical to hardness values than the effects of precipitation hardening. However, smaller grain sizes and more substructure reflect higher yield and tensile strength of parts produced by the Gaussian beam profile (Fig. 15). At a heat treatment temperature at 1154 °C, recrystallisation and grain growth occur. The initially larger grains in the ring-shaped beam profile sample further increase in size after recrystallisation, resulting in slightly larger crystalline grains and consequently somewhat inferior mechanical properties and hardness.

The shape and distribution of pores in the ring-shaped beam profile sample may be less favourable, leading to slightly poorer properties in both horizontal and vertical directions. Generally, the properties of PBF-LB/M-processed metallic samples are better in the horizontal direction [61]. During heat treatment, the Laves phase dissolves, and the δ-phase forms, often growing directly on the Laves phase (Fig. 6). In the case of directionally oriented dendrites in the build direction of the sample, this also leads to directional precipitation of the δ-phase. Since the δ-phase strengthens the microstructure, this can result in better mechanical properties in the vertical direction than the horizontal, significantly affecting the yield strength. Higher annealing temperatures lead to a smaller amount of δ-phase, which consequently means more Nb is available for fine γ' and γ'' precipitates. Finer γ' and γ'' precipitates in larger volumes are more effective barriers to dislocation mobility than the δ-phase. Based on TEM analysis (Figs. 12 and 13), it is evident that different beam profiles have no significant influence on the size and distribution of γ' and γ'' precipitates. This is why average yield strength (Fig. 15a and b) and hardness (Fig. 17) increase for the parts annealed at 984 °C and 1034 °C. However, due to softening mechanisms, the average tensile strength decreased with an increased annealing temperature. All those mechanisms overlap here, influencing the hardness, yield strength and ultimate tensile strength. In general, it could be concluded that the optimal heat treatment temperature for both investigated beam shapes is around 984 °C. At higher heat treatment temperature (around 1034 °C) is beneficial for achieving maximum yield strength values. The mechanical test results, specifically elongation and contraction, are quite poor for the ring beam shape at temperatures of 954 °C and 1034 °C in the vertical direction, which is related to the porosity found on the fracture surfaces (Fig. 16). Despite the fact that the porosity of samples produced with the ring beam profile is only slightly higher, this significantly affects their mechanical properties, especially in the vertical direction. The input enthalpy relative to the hatch distance is very similar for both beam profiles. The ring beam profile has slightly lower input enthalpy, which is likely the reason for the somewhat higher porosity.

For demanding applications hot isostatic pressing (HIP) is quite often a necessary step in PBF-LB/M to reduce porosity. It is conducted in a temperature range between 1120 °C and 1260 °C [45,62]before the heat treatment process. Based on the present study and the literature source [60], it can be observed that recrystallisation already occurs above the temperature of 1050 °C. Thus, it is impossible to achieve a non-recrystallised microstructure with fined grains and without MC carbides, which form above the temperature of 1050 °C [54]. Based on our research findings, the samples produced with a ring-shaped beam profile, due to its distinct melt pool configuration and resulting temperature gradient, likely lead to less pronounced segregation, particularly along dendritic boundaries. These boundaries are the source of excess Nb and Ti elements, contributing to Nb and Ti carbonitrides forming during heat treatment above the lowest possible HIP temperature.

5. Conclusions

This study comprehensively examines the impact of two distinct laser beam profiles in the PBF-LB/M process on microstructure development. This includes analysis in both the as-built state and after various post-heat treatments as well as the correlation between microstructural changes and mechanical properties. Based on the results, we establish an optimised heat treatment temperature for the investigated laser beam profiles. The investigation leads to the following conclusions.

- The optimal heat treatment temperature for both laser beam shapes is around 984 °C. At this temperature, the tensile strength values equalise in horizontal and vertical build directions. The yield strength values also increase, which is desirable for most applications.
- Heat treatment at temperatures above the recrystallisation point leads to a reduction in mechanical properties and hardness, primarily due to an increase in crystalline grain size. Additionally, (Nb, Ti) carbides grow or new ones form, which is undesirable in the microstructure.
- The key difference in microstructure between the heat treatment temperatures of 1034 °C and 1154 °C is that at 1154 °C, recrystallisation occurs, leading such high temperatures also to the growth of existing carbides and the formation of new ones.
- In addition to enabling faster printing, the ring-shaped beam profile offers a significant advantage by reducing carbide formation at higher heat treatment temperatures. By slowing the cooling rate, this profile reduces the segregation of carbide-forming elements. This is particularly important for products requiring HIP processing, where recrystallisation and carbide formation are unavoidable.

Data availability

The data is available in the Zenodo repository: 10.5281/zenodo.14163786.

Declaration of competing interest

The authors declare that they have no known competing financial interests or personal relationships that could have appeared to influence the work reported in this paper.

Acknowledgement

This work was funded by the EU Research and Innovation funding programme Horizon Europe (project InShaPe - Green Additive Manufacturing through Innovative Beam Shaping and Process

Monitoring, Project No. 101058523). The authors also thank the Slovenian Research and Innovation Agency (core funding Nos. P2-0132 and P2-0050 and Infrastructure Programme I0-0006) for the financial support.

References

[1] Ghaemifar S, Mirzadeh H. Dissolution kinetics of Laves phase during homogenization heat treatment of additively manufactured Inconel 718 superalloy. J Mater Res Technol 2023;24:3491–501. https://doi.org/10.1016/j.jmrt.2023.04.013.

[2] Kaleli Alay T, Cagirici M, Yalcin MY, Yagmur A, Tirkes S, Aydogan E, et al. Tailoring the microstructure and mechanical properties of IN718 alloy via a novel scanning strategy implemented in laser powder bed fusion. Mater Sci Eng, A 2023;884:145543. https://doi.org/10.1016/j.msea.2023.145543.

[3] Chen Y, Guo Y, Xu M, Ma C, Zhang Q, Wang L, et al. Study on the element segregation and Laves phase formation in the laser metal deposited IN718 superalloy by flat top laser and Gaussian distribution laser. Mater Sci Eng, A 2019;754:339–47. https://doi.org/10.1016/j.msea.2019.03.096.

[4] International Standard ISO/ASTM 52900. Additive manufacturing - general principles. Switzerland n.d: Fundamentals and vocabulary; 2021.

[5] Trosch T, Strößner J, Völkl R, Glatzel U. Microstructure and mechanical properties of selective laser melted Inconel 718 compared to forging and casting. Mater Lett 2016;164:428–31. https://doi.org/10.1016/j.matlet.2015.10.136.

[6] Švec M, Solfronk P, Nováková I, Sobotka J, Moravec J. Comparison of the structure, mechanical properties and effect of heat treatment on alloy inconel 718 produced by conventional technology and by additive layer manufacturing. Materials 2023;16. https://doi.org/10.3390/ma16155382.

[7] Zhou L, Mehta A, McWilliams B, Cho K, Sohn Y. Microstructure, precipitates and mechanical properties of powder bed fused inconel 718 before and after heat treatment. J Mater Sci Technol 2019;35:1153–64. https://doi.org/10.1016/j.jmst.2018.12.006.

[8] Rielli VV, Piglione A, Pham M-S, Primig S. On the detailed morphological and chemical evolution of phases during laser powder bed fusion and common post-processing heat treatments of IN718. Addit Manuf 2022;50:102540. https://doi.org/10.1016/j.addma.2021.102540.

[9] Zhu L, Xu ZF, Liu P, Gu YF. Effect of processing parameters on microstructure of laser solid forming Inconel 718 superalloy. Opt Laser Technol 2018;98:409–15. https://doi.org/10.1016/j.optlastec.2017.08.027.

[10] Wang K, Liu Y, Sun Z, Lin J, Lv Y, Xu B. Microstructural evolution and mechanical properties of Inconel 718 superalloy thin wall fabricated by pulsed plasma arc additive manufacturing. J Alloys Compd 2020;819:152936. https://doi.org/10.1016/j.jallcom.2019.152936.

[11] Huang W, Yang J, Yang H, Jing G, Wang Z, Zeng X. Heat treatment of Inconel 718 produced by selective laser melting: microstructure and mechanical properties. Mater Sci Eng, A 2019;750:98–107. https://doi.org/10.1016/j.msea.2019.02.046.

[12] Chlebus E, Gruber K, Kuźnicka B, Kurzac J, Kurzynowski T. Effect of heat treatment on the microstructure and mechanical properties of Inconel 718 processed by selective laser melting. Mater Sci Eng, A 2015;639:647–55. https://doi.org/10.1016/j.msea.2015.05.035.

[13] Wang Z, Guan K, Gao M, Li X, Chen X, Zeng X. The microstructure and mechanical properties of deposited-IN718 by selective laser melting. J Alloys Compd 2012;513:518–23. https://doi.org/10.1016/j.jallcom.2011.10.107.

[14] Zhao Y, Guan K, Yang Z, Hu Z, Qian Z, Wang H, et al. The effect of subsequent heat treatment on the evolution behavior of second phase particles and mechanical properties of the Inconel 718 superalloy manufactured by selective laser melting. Mater Sci Eng, A 2020;794:139931. https://doi.org/10.1016/j.msea.2020.139931.

[15] Xie H, Yang K, Li F, Sun C, Yu Z. Investigation on the Laves phase formation during laser cladding of IN718 alloy by CA-FE. J Manuf Process 2020;52:132–44. https://doi.org/10.1016/j.jmapro.2020.01.050.

[16] Farias FWC, Duarte VR, Filho J da CP, Figueiredo AR, Schell N, Maawad E, et al. High-performance Ni-based superalloy 718 fabricated via arc plasma directed energy deposition: effect of post-deposition heat treatments on microstructure and mechanical properties. Addit Manuf 2024;88. https://doi.org/10.1016/j.addma.2024.104252.

[17] Ghaemifar S, Mirzadeh H. Precipitation kinetics of niobium carbide (NbC) during homogenization heat treatment of additively manufactured inconel 718 superalloy. J Mater Res Technol 2023;25:1774–81. https://doi.org/10.1016/j.jmrt.2023.06.069.

[18] Kuo C-M, Yang Y-T, Bor H-Y, Wei C-N, Tai C-C. Aging effects on the microstructure and creep behavior of Inconel 718 superalloy. Mater Sci Eng, A 2009;510–511:289–94. https://doi.org/10.1016/j.msea.2008.04.097.

[19] Jansen D, Hanemann T, Radek M, Rota A, Schröpfer J, Heilmaier M. Development of actual powder layer height depending on nominal layer thicknesses and selection of laser parameters. J Mater Process Technol 2021;298:117305. https://doi.org/10.1016/j.jmatprotec.2021.117305.

[20] Montero-Sistiaga ML, Godino-Martinez M, Boschmans K, Kruth J-P, Van Humbeeck J, Vanmeensel K. Microstructure evolution of 316L produced by HP-SLM (high power selective laser melting). Addit Manuf 2018;23:402–10. https://doi.org/10.1016/j.addma.2018.08.028.

[21] Zhao C, Bai Y, Zhang Y, Wang X, Xue JM, Wang H. Influence of scanning strategy and building direction on microstructure and corrosion behaviour of selective laser melted 316L stainless steel. Mater Des 2021;209:109999. https://doi.org/10.1016/j.matdes.2021.109999.

[22] Ni C, Zhu L, Zheng Z, Zhang J, Yang Y, Hong R, et al. Effects of machining surface and laser beam scanning strategy on machinability of selective laser melted Ti6Al4V alloy in milling. Mater Des 2020;194:108880. https://doi.org/10.1016/j.matdes.2020.108880.

[23] Wang Y, Shi J. Influence of laser scan speed on micro-segregation in selective laser melting of an iron-carbon alloy: a multi-scale simulation study. Procedia Manuf 2018;26:941–51. https://doi.org/10.1016/j.promfg.2018.07.121.

[24] Guo W, Feng B, Yang Y, Ren Y, Liu Y, Yang H, et al. Effect of laser scanning speed on the microstructure, phase transformation and mechanical property of NiTi alloys fabricated by LPBF. Mater Des 2022;215:110460. https://doi.org/10.1016/j.matdes.2022.110460.

[25] Shi R, Khairallah SA, Roehling TT, Heo TW, McKeown JT, Matthews MJ. Microstructural control in metal laser powder bed fusion additive manufacturing using laser beam shaping strategy. Acta Mater 2020;184:284–305. https://doi.org/10.1016/j.actamat.2019.11.053.

[26] Matthews MJ, Roehling TT, Khairallah SA, Tumkur TU, Guss G, Shi R, et al. Controlling melt pool shape, microstructure and residual stress in additively manufactured metals using modified laser beam profiles. Proced CIRP 2020;94:200–4. https://doi.org/10.1016/j.procir.2020.09.038.

[27] Nadammal N, Cabeza S, Mishurova T, Thiede T, Kromm A, Seyfert C, et al. Effect of hatch length on the development of microstructure, texture and residual stresses in selective laser melted superalloy Inconel 718. Mater Des 2017;134:139–50. https://doi.org/10.1016/j.matdes.2017.08.049.

[28] McLouth TD, Witkin DB, Bean GE, Sitzman SD, Adams PM, Lohser JR, et al. Variations in ambient and elevated temperature mechanical behavior of IN718 manufactured by selective laser melting via process parameter control. Mater Sci Eng, A 2020;780:139184. https://doi.org/10.1016/j.msea.2020.139184.

[29] Fayed EM, Saadati M, Shahriari D, Brailovski V, Jahazi M, Medraj M. Optimization of the post-process heat treatment of inconel 718 superalloy fabricated by laser powder bed fusion process. Metals 2021;11. https://doi.org/10.3390/met11010144.

[30] Diepold B, Vorlaufer N, Neumeier S, Gartner T, Göken M. Optimization of the heat treatment of additively manufactured Ni-base superalloy IN718. Int J Miner Metall Mater 2020;27:640–8. https://doi.org/10.1007/s12613-020-1991-6.

[31] Schröder J, Mishurova T, Fritsch T, Serrano-Munoz I, Evans A, Sprengel M, et al. On the influence of heat treatment on microstructure and mechanical behavior of laser powder bed fused Inconel 718. Mater Sci Eng, A 2021;805:140555. https://doi.org/10.1016/j.msea.2020.140555.

[32] Lo Y-L, Liu B-Y, Tran H-C. Optimized hatch space selection in double-scanning track selective laser melting process. Int J Adv Des Manuf Technol 2019;105:2989–3006. https://doi.org/10.1007/s00170-019-04456-w.

[33] Carraturo M, Lane B, Yeung H, Kollmannsberger S, Reali A, Auricchio F. Numerical evaluation of advanced laser control strategies influence on residual stresses for laser powder bed fusion systems. Integr Mater Manuf Innov 2020;9:435–45. https://doi.org/10.1007/s40192-020-00191-3.

[34] Galbusera F, Caprio L, Previtali B, Demir AG. The influence of novel beam shapes on melt pool shape and mechanical properties of LPBF produced Al-alloy. J Manuf Process 2023;85:1024–36. https://doi.org/10.1016/j.jmapro.2022.12.007.

[35] Galbusera F, Caprio L, Previtali B, Demir AG. Analytical modeling and characterization of ring beam profiles for high-power lasers used in industrial manufacturing. J Manuf Process 2024;117:387–404. https://doi.org/10.1016/j.jmapro.2024.02.069.

[36] Okunkova A, Volosova M, Peretyagin P, Vladimirov Y, Zhirnov I, Gusarov AV. Experimental approbation of selective laser melting of powders by the use of non-Gaussian power density distributions. Phys Procedia 2014;56:48–57. https://doi.org/10.1016/j.phpro.2014.08.095.

[37] Matthews MJ, Roehling TT, Khairallah SA, Guss G, Wu SQ, Crumb MF, et al. Spatial modulation of laser sources for microstructural control of additively manufactured metals. Proced CIRP 2018;74:607–10. https://doi.org/10.1016/j.procir.2018.08.077.

[38] Bi J, Wu L, Li S, Yang Z, Jia X, Starostenkov MD, et al. Beam shaping technology and its application in metal laser additive manufacturing: a review. J Mater Res Technol 2023;26:4606–28. https://doi.org/10.1016/j.jmrt.2023.08.037.

[39] Sanaei N, Fatemi A. Defects in additive manufactured metals and their effect on fatigue performance: a state-of-the-art review. Prog Mater Sci 2021;117:100724. https://doi.org/10.1016/j.pmatsci.2020.100724.

[40] Chen B, Zhuo L, Xie Y, Huang S, Wang T, Yan T, et al. Comparative study on microstructure, mechanical and high temperature oxidation resistant behaviors of SLM IN718 superalloy before and after heat treatment. J Mater Res Technol 2024;31:1535–46. https://doi.org/10.1016/j.jmrt.2024.06.163.

[41] Holla V, Kopp P, Grünewald J, Wudy K, Kollmannsberger S. Laser beam shape optimization in powder bed fusion of metals. Addit Manuf 2023;72:103609. https://doi.org/10.1016/j.addma.2023.103609.

[42] Mirzabeigi N, Holfelder-Schwalme P, He Y, Wudy K. Tailored microstructure in laser-based powder bed fusion of IN718 through novel beam shaping technology. J Laser Appl 2024;36:42070. https://doi.org/10.2351/7.0001623.

[43] Bayat M, Rothfelder R, Schwarzkopf K, Zinoviev A, Zinovieva O, Spurk C, et al. Exploring spatial beam shaping in laser powder bed fusion: high-fidelity simulation and in-situ monitoring. Addit Manuf 2024;93:104420. https://doi.org/10.1016/j.addma.2024.104420.

[44] Pérez-Ruiz JD, Galbusera F, Caprio L, Previtali B, Lacalle LNL de, Lamikiz A, et al. Laser beam shaping facilitates tailoring the mechanical properties of IN718 during powder bed fusion. J Mater Process Technol 2024;328:118393. https://doi.org/10.1016/j.jmatprotec.2024.118393.

[45] ASTM Standard. F3055-14AR21 "standard specification for additive manufacturing nickel alloy (UNS N07718) with powder bed fusion. West Conshohocken, PA: ASTM International; 2021. https://doi.org/10.1520/F3055-14AR21. USA n.d.
[46] Holfelder Peter, Witte Armin. United States Patent No. US20210387284A1, n.d. 2019-11-05.
[47] Grünewald J, Wudy K. Dimensionless process windows in laser-based powder bed fusion of AISI 316L using ring-shaped beam profiles. Addt Manuf Lett 2025;14: 100284. https://doi.org/10.1016/j.addlet.2025.100284.
[48] International standard ISO 6892-1. Switzerland: Metallic materials - Tensile testing - Part 1: Method of test at room temperature; 2019 [n.d.].
[49] Bruce D, Paradise P, Saxena A, Temes S, Clark R, Noe C, et al. A critical assessment of the Archimedes density method for thin-wall specimens in laser powder bed fusion: measurement capability, process sensitivity and property correlation. J Manuf Process 2022;79:185–92. https://doi.org/10.1016/j.jmapro.2022.04.059.
[50] International standard ISO 6507-1. Switzerland: Metallic materials - Vickers hardness test Part 1: Test method; 2023 [n.d].
[51] Haines MP, Rielli VV, Primig S, Haghdadi N. Powder bed fusion additive manufacturing of Ni-based superalloys: a review of the main microstructural constituents and characterization techniques. J Mater Sci 2022;57:14135–87. https://doi.org/10.1007/s10853-022-07501-4.
[52] Donik Č, Kraner J, Paulin I, Godec M. Influence of the energy density for selective laser melting on the microstructure and mechanical properties of stainless steel. Metals 2020;10. https://doi.org/10.3390/met10070919.
[53] Zhang S, Wang L, Lin X, Yang H, Huang W. The formation and dissolution mechanisms of Laves phase in Inconel 718 fabricated by selective laser melting compared to directed energy deposition and cast. Compos B Eng 2022;239:109994. https://doi.org/10.1016/j.compositesb.2022.109994.
[54] Ferreri NC, Vogel SC, Knezevic M. Determining volume fractions of γ, γ′, γ″, δ, and MC-carbide phases in Inconel 718 as a function of its processing history using an advanced neutron diffraction procedure. Mater Sci Eng, A 2020;781:139228. https://doi.org/10.1016/j.msea.2020.139228.
[55] Godec M, Zaefferer S, Podgornik B, Šinko M, Tchernychova E. Quantitative multiscale correlative microstructure analysis of additive manufacturing of stainless steel 316L processed by selective laser melting. Mater Char 2020;160: 110074. https://doi.org/10.1016/j.matchar.2019.110074.
[56] Rizwan M, Ullah R, Lu J, Wang J, Zhang Y, Zhang Z. Insight into elongation and strength enhancement of heat-treated LPBF Ni-based superalloy 718 using in-situ SEM-EBSD. Mater Sci Eng, A 2024;914. https://doi.org/10.1016/j.msea.2024.147163.
[57] Bayat M, Zinovieva O, Zinoviev A, Rothfelder R, Scharwzkopf K, Schmidt M, et al. Understanding the thermo-fluid-microstructural impact of beam shaping in Laser Powder Bed Fusion using high-fidelity multiphysics simulation. Proced CIRP 2024; 124:358–61. https://doi.org/10.1016/j.procir.2024.08.133.
[58] Wang J, Zhu R, Liu Y, Zhang L. Understanding melt pool characteristics in laser powder bed fusion: an overview of single- and multi-track melt pools for process optimization. Adv Power Mater 2023;2:100137. https://doi.org/10.1016/j.apmate.2023.100137.
[59] Hu H, Pan Y, Hu L, Du D, Wang S, Wen J-F, et al. Microstructure instability of additively manufactured alloy 718 fabricated by laser powder bed fusion during thermal exposure at 600–1000 °C. J Alloys Compd 2025;1010:177316. https://doi.org/10.1016/j.jallcom.2024.177316.
[60] Krek Gašper. Characterization of heat-treated nickel-based superalloy Inconel 718 manufactured by laser powder bed fusion : master's thesis. 2024 [online], [Accessed 29 October 2024].
[61] Gallmeyer TG, Moorthy S, Kappes BB, Mills MJ, Amin-Ahmadi B, Stebner AP. Knowledge of process-structure-property relationships to engineer better heat treatments for laser powder bed fusion additive manufactured Inconel 718. Addit Manuf 2020;31:100977. https://doi.org/10.1016/j.addma.2019.100977.
[62] Gruber K, Stopyra W, Kobiela K, Madejski B, Malicki M, Kurzynowski T. Mechanical properties of Inconel 718 additively manufactured by laser powder bed fusion after industrial high-temperature heat treatment. J Manuf Process 2022;73: 642–59. https://doi.org/10.1016/j.jmapro.2021.11.053.